

# Spatio-temporal ultrawideband indoor propagation modelling by reduced complexity geometric optics

W.Q. Malik, C.J. Stevens and D.J. Edwards

**Abstract:** A simple and efficient virtual-source ray-tracing technique for the simulation of indoor wideband radio and optical propagation channels is proposed. The parametric deterministic model considers the room geometry, transceiver locations, material properties and probe signal types. It is applied to the indoor ultrawideband channel in the FCC-allocated 3.1–10.6 GHz band, and a range of novel results are presented to illustrate several possible applications. The channel small-scale fading statistics and spatial variability are examined by synthesising a densely sampled aperture. Multiple-antenna array systems are simulated to evaluate multiple-input multiple-output performance. The multipath angular characteristics are analysed from the simulated azimuth-delay profile. The simulation results closely match previous channel measurement studies and statistical models, validating the proposed technique. It is shown that specular reflection is dominant, and power convergence is achieved with three reflections in a typical indoor environment. Thus, it is demonstrated that despite its simplicity, the model yields reliable and accurate results, and can therefore be a useful tool for indoor wireless network planning and performance prediction.

## 1 Introduction

Optical ray-tracing is frequently employed for deterministic channel modelling and simulation in situations where the propagation environment geometry is well known. It is based on the solution of Maxwell's equations with high-frequency approximations. Traditional ray-tracing uses the knowledge of the locations and electromagnetic properties of scattering objects to calculate the resultant electric field at the receiver using image theory [1, 2]. Electromagnetic waves conform to ray behaviour at microwave frequencies [3]. Non-specular signal components and other complex effects can therefore be neglected, for instance, for a typical brick wall at frequencies below 20 GHz, without a significant loss of accuracy [4, 5]. Thus, simple indoor radio propagation models usually consider purely specular reflection. Some researchers have also considered wall textures in order to include the effect of scattering from objects with sub-wavelength dimensions [6]. From the Fraunhofer criterion for flat surfaces, however, scattering is negligible across the microwave frequency range and is important only for millimeter waves [4]. Diffraction is taken into account by some ray-tracing models [7], but it can also be ignored for microwave and higher frequency signals propagating in indoor channels [8]. Conventional ray-tracing, which approximates sinusoidal plane waves as rays, is applicable only to narrow-band signals. The technique was extended to ultrawideband (UWB) channels [9] by the superposition of ray-tracing for the individual frequency components in [10]. An alternative time-domain approach, based on the addition of the impulse responses of individual rays, was presented in [11].

Exhaustive ray-tracing methods provide an accurate estimate of the channel in complex environments. They are, however, computationally intensive and thus often impractical for simulating systems with large complexity, such as UWB channels, multiple-input multiple-output (MIMO) channels or synthetic aperture radar imaging. In recursive ray-launching or shoot-and-bounce schemes [12], rays are launched from the transmitter in all directions, intersecting surrounding objects and undergoing transmission or reflection, with a point of reflection considered a secondary source. The more efficient virtual source (VS) techniques, based on the method of images, treat objects as mirrors and determine the locations of transmitter images behind them to be treated as secondary sources. A hierarchical structure of sources is created with the transmitter at its root and each level representing a reflection order. Thus, the presence of a ray-path is determined for a given receiver location. The preprocessing of location visibility trees [13] or illumination zones for a given transmitter position [12–14] can improve the runtime efficiency to some extent.

Ray-tracing models can predict radio system performance using the specified propagation characteristics, while measurement-based models depend greatly on the available experimental conditions. Our model, which in essence uses a multivariate description of the channel, utilises the information about a variety of important propagation parameters that are generally ignored by many of the existing statistical models, and may therefore provide more accurate results. Additionally, practical constraints allow the experimental investigation of only a small number of propagation parameters, which is a limiting factor for measurement-based propagation environmental analysis capability and system performance prediction accuracy. In contrast, a model that allows detailed signal and environment specification can facilitate more comprehensive channel characterisation, with the additional benefit of efficiency and convenience. These factors motivate the development of a deterministic radio channel prediction model in the current paper.

## 2 Channel prediction technique

A cuboidal room-tiling model is used for the simulation of the short-range indoor channel in our technique. It provides an efficient means of simulating the indoor UWB channel although with a loss of accuracy in the site-specific modelling of complex environments. In this method, virtual rooms extend in an infinite 3D space containing VS that are images of the actual source reflected in the room's surfaces. The high computational efficiency of this technique is achieved at the cost of the ability to specify an irregular room geometry, locations of scattering and obstructing objects, non-homogeneous material properties and other fine details.

Typical wireless personal area networks involve vertically polarised antennas with omni-directional azimuthal radiation patterns and nulls at high elevation, which leads to predominantly azimuthal signal propagation [15]. Analytical, stochastic and deterministic models are therefore often simplified by considering only two-dimensional propagation; this approximation has been used in the ray-tracing models in [1, 16], for instance. The techniques developed in the current paper also use this assumption, and are based on rectangular room-tiling in the infinite horizontal space. The concept is illustrated in Fig. 1, where the central rectangular region represents the actual room and the surrounding extensions contain the virtual sources,  $VS_n$ , arising due to wall reflections.

For the reasons discussed above, specular reflection is considered in the model while diffraction and scattering are neglected, so that every wave component traverses one of more freespace propagation paths between the transmitter and the receiver. The model can simulate line-of-sight (LOS), obstructed-line-of-sight (OLOS) and non-line-of-sight (NLOS) scenarios; the direct path blockage for the OLOS and NLOS scenarios can be simulated by artificially attenuating or excising the first arrival from the channel impulse response. The results in this paper will be limited to the LOS scenario, which is encountered more commonly in indoor communications applications.

The proposed parametric model allows the specification of the probe signal waveform type, frequency band, transmitter and receiver locations, room dimensions, wall reflection coefficient, maximum reflection order, power-delay profile (PDP) threshold and additive noise variance. It can also easily be extended to include various other factors

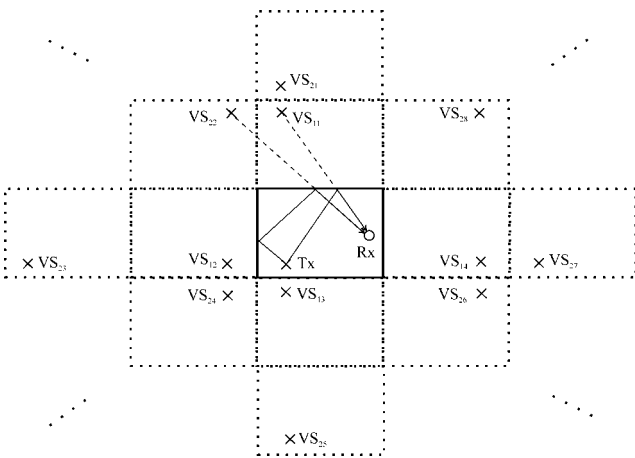


**Fig. 1** Two-dimensional ray-tracing model based on the method of images

$VS_{ab}$  represent the virtual sources, where  $b$  is the index to the VS for the  $a$ th reflection order. Two of the reflected ray paths, back-propagated to the corresponding VS, are shown

that affect signal propagation, such as electromagnetic polarisation of the signals and antenna radiation patterns.

The reflection order,  $K$ , refers to the maximum number of reflections considered in the model per wave component. This parameter increases the complexity of a given ray-tracing model, but a low order usually suffices for the modelling of realistic radio channels. The proposed two-dimensional model generates a total of  $N$  VS for order  $K$ . From Fig. 1 and the method of images, it is straight-forward to see that

$$N = l + \sum_{k=1}^K 4k \quad (1)$$

where  $l = \{0, 1\}$  for NLOS and LOS conditions, respectively, and the second term in (1) is due to multipath. The complex electric field incident at the receiver due to the  $n$ th impinging wave is a function of the number of reflections,  $P_n$ , and the composite pathlength,  $d_n$ . This pathlength is defined as

$$d_n = \sum_{p=1}^{P_n} d_{n,p}$$

where  $d_{n,p}$  is the distance traversed by the specular wave between the  $(p-1)$ th and  $p$ th boundary intersections. The received signal due to the  $n$ th wave can thus be represented as

$$\tilde{E}_n = E_0 A(d_n) \prod_{p=1}^{P_n} \Gamma_p e^{-j2\pi d_{n,p}/\lambda_c} \quad (2)$$

where  $E_0$  is the transmitted electric field,  $\Gamma_p$  is the wall reflection coefficient for the  $p$ th wave-interface intersection, and

$$A(d_n) = \frac{\lambda_c}{4\pi d_n} \quad (3)$$

is the freespace pathloss, assuming omni-directional antennas where the azimuthal-plane antenna gains have been ignored for simplicity.

It should be noted that (2) can be interpreted as analogous to the Motley–Keenan indoor propagation model, which suggests that the average pathloss can be decomposed into a free-space pathloss component and a factor determined by the number of walls between the transmitter and the receiver [17]. The exponential term in (2) represents the propagation phase offset due to the pathlength  $d_n$ ,  $p$ , and implicitly models wave interference and the consequent local multipath fading. While frequency-dependent pathloss leads to UWB waveform distortion and receiver correlation loss [18], we neglect this effect here as our current analysis does not involve powerloss behaviour. The wavelength  $\lambda_c$ , corresponding to the centre frequency  $f_c = 6.85$  GHz, is thus used here for simplicity. Perfectly vertical, smooth and uniformly reflective walls are assumed. The fractional power transmission is assumed to be independent of the angle of incidence. As all material interactions are identical due to these assumptions, we can rewrite (2) as

$$\tilde{E}_n = E_0 A(d_n) \Gamma^{P_n} e^{-j2\pi d_n/\lambda_c} \quad (4)$$

where  $\Gamma$  is now the uniform reflection coefficient of the walls. Thus only the number of ray–wall intersections is important in this model, and not the intersection coordinates. This is one of the key factors leading to the reduction in the complexity of our algorithm as compared to other

ray-tracing schemes. The vector superposition of the  $N$  individual ray contributions gives the received signal, that is,

$$\tilde{E}_r = \sum_{n=1}^N \tilde{E}_n$$

The time-domain received signal, composed of  $N$  resolved multipath components, can be expressed mathematically as

$$r(t) = s(t) * h(t) + \eta(t)$$

after the removal of the propagation delay. Here  $s(t)$  is the transmitted signal waveform,  $n(t)$  is the additive noise, and

$$h(t) = \sum_{n=1}^N \alpha_n(t) \delta(t - t_n) e^{j\phi_n} \quad (5)$$

is the complex impulse response (CIR) of the channel, where  $\alpha_n$  is the amplitude of the  $n$ th multipath component,  $t_n$  its time delay and  $\phi_n$  its phase. From the linearity of the Fourier transform, the multipath waveforms may be superimposed in time or frequency. When  $\tilde{E}_n$  is a time-domain waveform, we have  $\tilde{E}_n = \alpha_n(t) \delta(t - t_n) e^{j\phi_n}$ , assuming an impulse transmission, which leads to the relation in (5).

### 3 Channel impulse response estimation

The following section illustrates the procedure for the extraction of the CIR and presents channel simulation results using the proposed ray-tracing model. To model realistic conditions with some signal leakage from the environment, we assume  $\Gamma = 0.5$ . In order to simulate a sufficiently reverberating environment,  $K = 5$  is used. Although any appropriate probing signal can be introduced, we use a Gaussian monocycle waveform, which is the derivative of a Gaussian function and has the functional form

$$s(t) = a \frac{t}{T} e^{-(t/T)^2} \quad (6)$$

where  $T$  is the decay constant and  $a$  is the amplitude. With a single time-domain zero-crossing and bandwidth spanning 3.1–10.6 GHz, the monocycle waveform is frequently used in UWB Impulse Radio communications and sensor networks [19, 20], and thus simulates the actual operating conditions in this model. The simulation parameters are summarised in Table 1. The sampling frequency,  $f_s = 22$  GHz, is selected to be over twice the highest signal frequency to meet the Nyquist sampling criterion. The dimensions of the room are designated as 6 m  $\times$  6 m, unless otherwise specified in the following sections, to simulate a typical indoor office environment so that the results can be verified against earlier measurement-based statistical studies. The antennas are assumed to be

**Table 1: Simulation parameters for ray-tracing**

Parameter	Symbol	Value
reflection coefficient	$\Gamma$	−3 dB
reflection order	$K$	5
probing signal type	$s(t)$	Gaussian monopulse
starting frequency	$f_i$	3.1 GHz
stop frequency	$f_h$	10.6 GHz
bandwidth	$B$	7.5 GHz
sampling frequency	$f_s$	22 GHz
PDP threshold	—	30 dB

omni-directional point sources, and their dispersive effects [21] are neglected.

The received signal is obtained as the superposition of the direct component and the specular components generated after the propagation of the Gaussian monocycle signal through the dispersive channel. The CIR in (5) is then obtained by deconvolving the transmitted signal  $s(t)$  from the received signal  $r(t)$  [22], that is,

$$h(t) = \int_{-f_s/2}^{f_s/2} \frac{R(f)}{S(f)} e^{j2\pi ft} df \quad (7)$$

where the spectra  $R(f)$  and  $S(f)$  are obtained from  $r(t)$  and  $s(t)$ , respectively, via the Fourier transform.

Fig. 2 exemplifies the channel prediction output of the model with the help of a typical CIR. As is customary, the time variable is transformed into time-delay through a translation by the propagation delay,  $t_p$ , of the first arrival, as the latter is not of interest in characterising the CIR. The exponential decay with time is due to the distance-dependent pathloss, which follows the inverse-square law for free-space propagation, for each multipath component. The deviations from this ideal behavior are caused due to lossy reflections from the walls that attenuate the specular components beyond the inverse-square factor. It is observed that a large number of resolvable paths, with some temporal sparsity, form distinct multipath clusters, in a manner similar to [23–25]. Some of the paths in each cluster are temporally proximal and thus may be unresolvable without sufficiently high-signal bandwidth and sampling rates. The multipath clusters are produced due to the minor differences in the pathlengths and flight times of the various propagation paths arising from a single scattering surface or from a single reflection order, with the inter-cluster delays determined by the room geometry and the locations of the transmitter and receiver. The reverberations last  $\sim 100$  ns in this channel realisation, with an exponential decay in power, which agrees closely with earlier measurement results for indoor UWB channels [24, 26].

A comparison of the CIRs generated at various receiving locations points to the random spatial variation in the multipath characteristics of the received signal. This effect is analysed quantitatively in the next section in the light of its impact on various channel and system performance

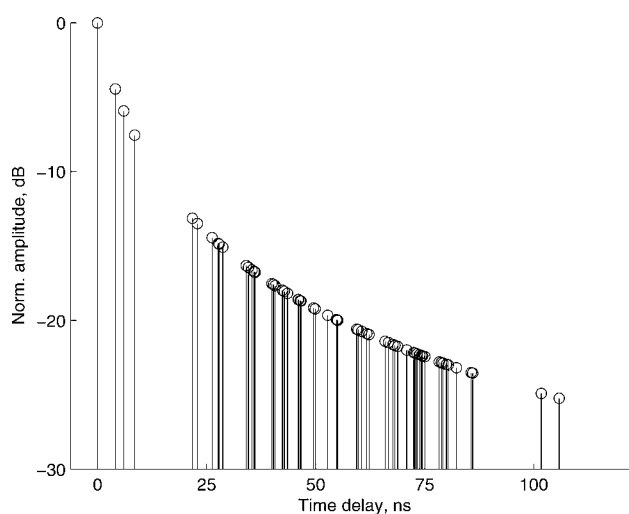


**Fig. 2** Peak-normalised complex impulse response at one location in an indoor environment, generated by ray-tracing, as a representative example

parameters, and the channel statistics generated over a large ensemble of realisations are evaluated.

## 4 Applications and results

We now consider a number of scenarios where the ray-tracing model of this paper can be advantageous for indoor channel characterisation. This section is primarily illustrative and does not attempt to present an exhaustive list of the possible applications. In this exemplification, a comparison of the results with measurement-based results is also presented, which serves to test the authenticity and benchmark the accuracy of the technique. As the proposed technique is computationally efficient, it is feasible for the generation of a large set of channel realisations at pre-determined or randomly selected locations within a room. This allows the collection of channel statistics over a large ensemble, as well as the investigation of spatial channel characteristics.

### 4.1 Small-scale fading statistics

We now use the model to synthesise an antenna aperture over a finite area by evaluating the corresponding CIRs. We define our rectangular coordinate system such that the bottom left corner of the room in Fig. 1 is located at the origin (0, 0), while the upper right-hand corner is at (6, 6), given the room dimensions, where the distance is in metres. Without loss of generality, the transmitter is placed at location  $\mathbf{r}_T = (1.4, 1)$ . A receiver aperture of dimensions  $\mathbf{r}_S = (1.5, 1.5)$  is synthesised by translating the receiving antenna, starting from location  $\mathbf{r}_R = (3.5, 4.1)$ , along both axes in 0.02 m steps. Thus the transmitter–receiver separation is  $\Delta r = 3.75$  m for the initial receive point, with the LOS present at all times, which resembles the IEEE 802.15.3a CM1 channel. Fig. 3 shows this simple illustrative scenario. This process, yielding a spatially distributed set of 5776 CIRs spanning  $1.5 \text{ m} \times 1.5 \text{ m}$ , can be used to analyze local channel variations, since each dimension of the area considered is approximately equivalent to  $15\lambda_l = 35\lambda_c = 53\lambda_h$ , where  $\lambda_l$ ,  $\lambda_c$ , and  $\lambda_h$  are the wavelengths corresponding to the lowest, centre and highest frequencies in our signal, respectively.

Thus, the spatial sampling provides a suitable estimate of the local channel characteristics for our UWB frequency range. A comparison of the fading statistics of the simulated channel with measurement results can be used to evaluate

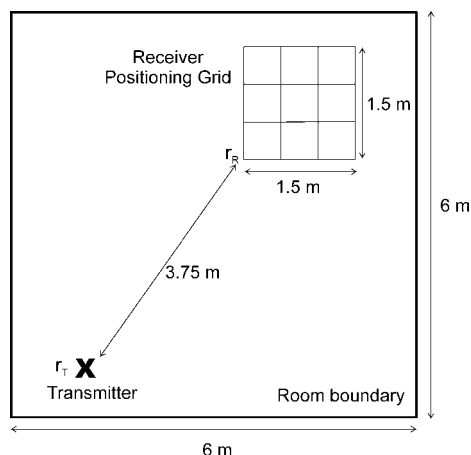


**Fig. 3** Simulation scenario for indoor small-scale variability analysis

the ray-tracing model accuracy as outlined in [27]. For this investigation, a local CIR ensemble is simulated and used to evaluate the channel statistics. Each CIR is thresholded to  $-30$  dB from its peak level to include only the significant power levels in further calculations [15]. The multipath delays are then extracted, and the delay spread statistics are evaluated. The RMS delay spread, important in channel characterisation, is defined as [15]

$$\tau_{\text{RMS}} = \sqrt{\frac{\sum_{\tau=0}^{\tau_s} (\tau - \bar{\tau})^2 |h(\tau)|^2}{\sum_{\tau=0}^{\tau_s} |h(\tau)|^2}} \quad (8)$$

where  $\bar{\tau}$  denotes the mean excess delay and  $\tau_s$  the maximum excess delay. The statistics of the mean excess delay maximum excess delay and RMS delay spread, for the CIRs simulated as above are listed in Table 2. The channel statistics obtained from ray-tracing correspond well to those obtained from measurement in [28–31], with slight variations that arise due to the specific experimental conditions as well as the presence of scattering objects within the room in dense multipath environments. The small-scale fading parameters, for example, the delay spread and number of paths from our simulation are also found to conform to the IEEE 802.15.3a CM1 channel model [32] when similar propagation conditions are created. The proposed model is therefore a reliable tool for indoor UWB channel simulation. Also, this comparison provides evidence that specular reflection is the dominant propagation mode, and the contribution of diffraction, refraction and scattering can be neglected.

### 4.2 Spatial variability

Synthetic aperture simulation is next used to predict the local spatial variation in system performance by evaluating some of the small-scale fading parameters. The resulting patterns, shown in Fig. 4, agree closely with previous experimental [33, 34] and stochastic [35] models.

The coherent interference of multipath components leads to small-scale fading and spatial variation in the PDP, altering such statistical descriptors as the RMS delay spread and number of resolved paths over a small area. The consequent interference fringes are arranged predominantly across the cross-range direction or along the wavefronts, while some are parallel to the room boundaries due to its rectangular symmetry, as evident from the simulated propagation scenario depicted in Fig. 3. With transceiver relocation, the paths fall in and out of a given time-delay bin, thereby altering the consequent channel response [36], which can physically be explained on the basis of the Lloyd's mirror phenomenon [37]. The  $\tau_{\text{RMS}}$  and  $N$  also generally undergo an increase with the transmitter–receiver separation, as noted from measurements in [28, 31].

**Table 2: Mean local fading characteristics of UWB channels from simulation and measurement [30, 32]**

Quantity	Ray-tracing	Measurement
RMS delay spread, ns	5.8	5.3
mean excess delay, ns	3.5	5.0
maximum excess delay, ns	44.4	50.6
number of paths	22.8	24

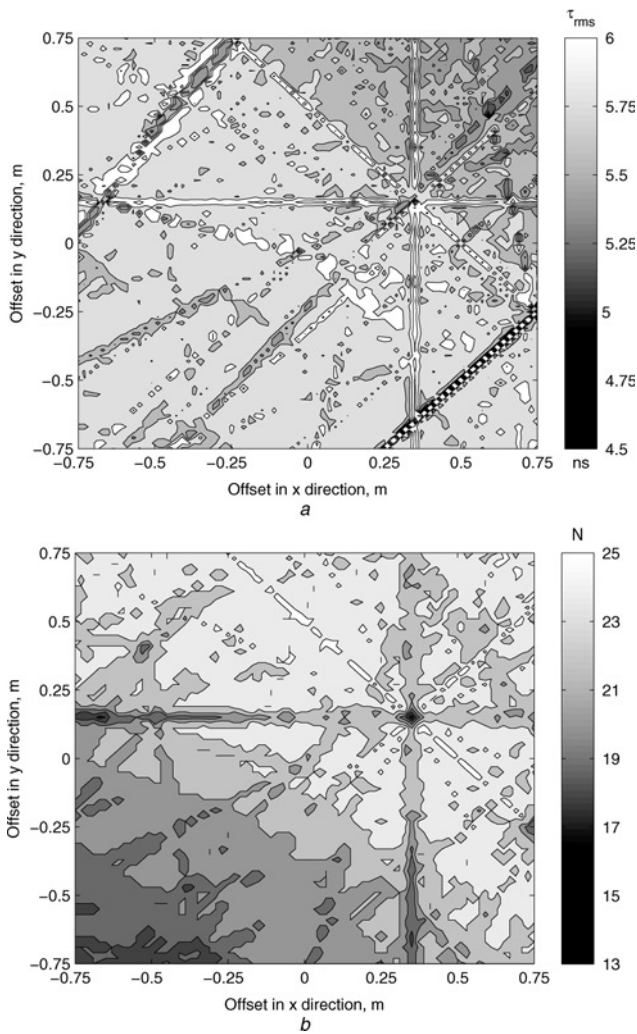


**Fig. 4** Simulated spatial distribution of small-scale fading statistics

a RMS delay spread  $\tau_{\text{RMS}}$   
b Number of received paths  $N$

In addition to small-scale fading characterisation, array synthesis can be used to extract information about the multipath directions-of-departure (DoD) and -arrival (DoA), with applications in single- and double-directional channel modelling, sensor localisation and ranging, beamforming and radio imaging using Huygen's backpropagation or super-resolution techniques [38].

### 4.3 Angular characterisation

The DoA and DoD information aids channel characterisation by identifying the distribution of scatterers in the environment, the consequent angular spread and other spatial properties of the channel. Coupled with the time-of-arrival information, it leads to full spatio-temporal channel characterisation. The angular multipath information can be extracted from our model using the knowledge of the transmitter and receiver locations and simple trigonometric rules. The VS locations are already available in the model, leading to the DoA for the signal arising from each VS. Similarly, it can be easily shown, given a rectangular room geometry, that the DoD is related to the DoA through simple trigonometric relations, and can therefore also be computed from the model. The estimation of the angular multipath information in this manner does not involve the aperture synthesis procedure discussed above

with dense sampling and large apertures, followed by image reconstruction techniques. Instead, it requires the CIR evaluation only at a single transmitter and receiver location instead of a range of adjacent locations, and is thus highly efficient. Our horizontal propagation model provides the angular channel profile in the azimuth ( $\varphi$ ) plane, while a 3D extension can be used to obtain the elevation ( $\theta$ ) information. The complete spherical coordinate ( $\varphi, \theta$ ) information for the DoAs and DoDs can then be used in conjunction with the PDP to construct a Minkowski space-time description of the channel in a simple and efficient manner. In the rest of this discussion, we restrict our analysis to azimuthal DoA profiles and present some illustrative results.

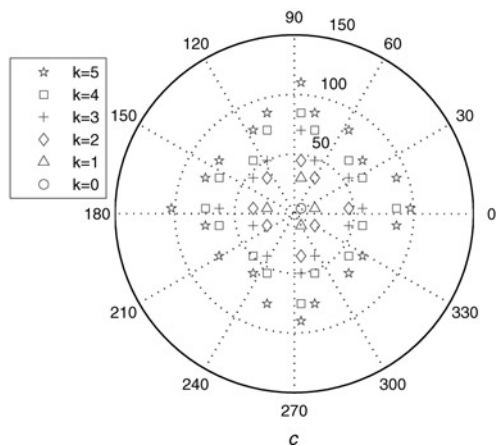
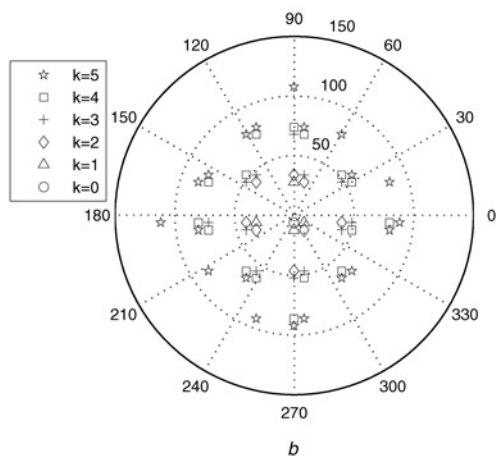
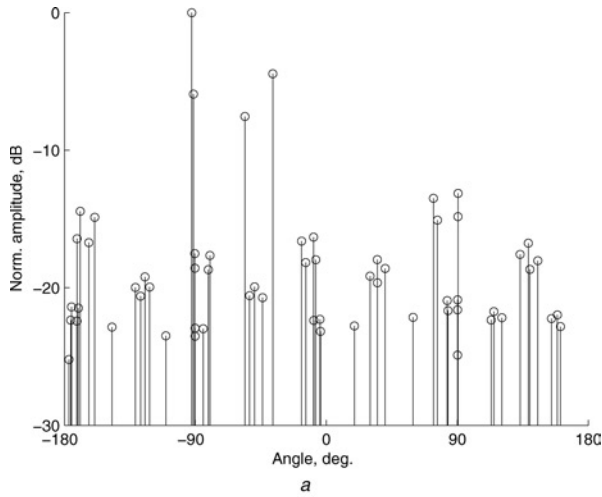
Consider a channel defined by transmitter location  $\mathbf{r}_T = (4.73, 0.9)$  and receiver location  $\mathbf{r}_R = (4.81, 2.74)$  in the same room as considered in the earlier analysis, where the coordinates are chosen randomly. The corresponding peak-normalised CIR is shown in Fig. 2. The corresponding power azimuth profile (PAP), represented by  $P_\varphi(\varphi)$ , provides information about the multipath DoAs and their gains. In the Cartesian coordinate system of Fig. 1, if  $(r_x, r_y)$  represents the coordinates of the receiver and  $(v_x^{(n)}, v_y^{(n)})$  represents the coordinates of the VS generating the  $n^{\text{th}}$  multipath component, the DoA of the  $n^{\text{th}}$  path with respect to the positive  $x$ -axis is given by  $\varphi_n = \tan^{-1}((v_y^{(n)} - r_y)/(v_x^{(n)} - r_x))$ .

Fig. 5a shows the PAP for the location under consideration, where the multipath gains are once again normalised to the direct path gain, which is incident at  $\varphi = -92^\circ$ . No noise thresholding is applied here and all paths generated with  $K = 5$  are shown. The specular components appear to arrive from a large range of directions without a particular pattern. This observation is found to be true for any randomly chosen transmitter–receiver location. Also from the figure, we can see that several of the DoAs are mutually proximal and produce angular multipath clusters. It is obvious that if the noise threshold in power calculation is reduced from 30 to, say, 20 dB, the number of significant paths and thus the range of DoAs will also decrease. The multipath gains in the PAP are identical to those in Fig. 2, but the ToA information is replaced by the angular information.

Further insight into the angular scattering process is provided by the azimuth delay-profile (ADP), denoted by  $P_{\tau,\varphi}(\tau, \varphi)$  and shown in Fig. 5b, which simultaneously considers the multipath DoA and ToA. In the polar plot shown, the ToA extends along the radial direction, the DoA is along the circular plot and the number of reflections a path has undergone is also indicated. While generally the path DoAs and ToAs are normalised with respect to those of the direct component, the propagation delay in Fig. 5b has not been removed from the ToA in order to preserve the directional information of the direct component being lost from plotting at the vertex.

A grid-like symmetry is observed in this figure, with the DoA–ToA points arranged along vertical and horizontal lines. Also, the points occur in clusters of four except at large ToAs where the arrivals become sparse and the reflections eventually die down. This symmetric pattern arises from the rectangular nature of the propagation environment, and is observed for all room dimensions and transmitter–receiver locations. Furthermore, within each four-element cluster, two of the diagonally opposite elements undergo the same number of reflections,  $k$ , while the remaining two undergo  $k - 1$  and  $k + 1$  reflections, respectively where  $k \geq 1$ . It is clear that if the multipath and angular resolution of the receiver is insufficient, it cannot differentiate

between the individual components within a cluster, which therefore appear collectively as a single, spread-out multipath component. The power of the component with the smallest number of reflections in the cluster, however, dominates in such a scenario, as it suffers the least attenuation. If the position of the transmitter or receiver is varied, the spread of the elements in the clusters varies, as illustrated by the ADP obtained with  $r_T = (4.26, 2.17)$  and  $r_T = (2.58, 0.8)$  shown in Fig. 5c, with the coordinates



**Fig. 5** Angular characterisation

a PDP at a single location whose CIR is given in Fig. 2  
b ADP at a single location whose CIR is shown in Fig. 2

c ADP at another location for comparison  
Radial dimension in the ADP plots shows the ToA in nanoseconds, the rotation depicts the DoA, and  $k$  is the number of reflections

again chosen randomly. It can be seen that the multipath quadruples have expanded, or the inter-arrival spread in each angular-temporal cluster has increased. Thus, the performance of an optimal, high complexity 2D rake, with time-delay and angular resolution capability, depends on its location within the environment.

The angular spread provides a quantitative description of the multipath clustering and the DoA distribution, and is thus important for the determination of spatial correlation, susceptibility to fading and channel capacity [39]. The RMS angular spread (RAS) is given by the expression

$$\varphi_{\text{RMS}} = \sqrt{\frac{\sum_{\varphi=-\pi}^{\pi} (\varphi - \bar{\varphi})^2 P_{\varphi}(\varphi)}{\sum_{\varphi=-\pi}^{\pi} P_{\varphi}(\varphi)}} \quad (9)$$

where  $\bar{\varphi}$  is the mean DoA. We evaluate the RAS for a set of 1000 simulated CIRs with the transmitter and receiver locations generated randomly in order to statistically characterise the angular spread in the indoor UWB channel. The  $\varphi_{\text{RMS}}$  predicted by this exercise is  $\sim 75^\circ$  and  $35^\circ$  when the noise threshold is 20 dB and 10 dB respectively. Earlier indoor UWB measurements in [40] reported smaller azimuthal scattering with  $\varphi_{\text{RMS}} = 38^\circ$ , but noted that the probable reason was an insufficient set of measurements and conjectured that if it were remedied, the angular spread would approach a uniform distribution. This was confirmed by further measurements that found angular scattering at wide angles [41, 42]. The ADP, obtained in the indoor UWB channel in general indicates that the multipath clusters are angularly uncorrelated, with the implication that spatial antenna diversity is expected to perform well in this environment even at antenna separations smaller than a half-wavelength. The azimuth-delay profile, and in turn the angular and delay spreads, strongly depend on transceiver locations in relation with the room geometry [43]. Thus, low spreads are observed closer to the corners of the room, due to angularly and temporally well-localised high-intensity clusters, than in the middle of the room.

#### 4.4 Large-scale pathloss

In order to characterise the large-scale fading behaviour in terms of pathloss, we generate a set of 1000 CIRs

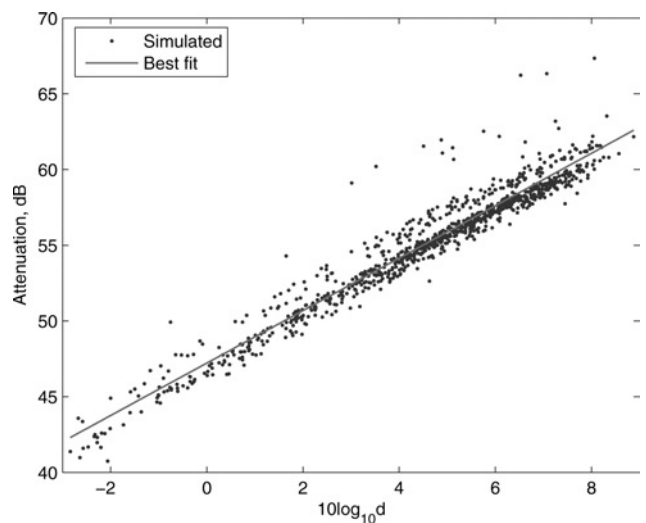


**Fig. 6** Regression of pathloss on distance in an indoor LOS environment

**Table 3: Predicted capacity of UWB multiple-antenna (SIMO and MIMO) systems at SNR = 10 dB in the indoor line-of-sight UWB channel from ray-tracing and measurement [9, 46]**

Array configuration	Array size	Ergodic capacity, bps/Hz		1% outage capacity, bps/Hz	
		Ray-tracing	Measurement	Ray-tracing	Measurement
SISO	1 × 1	3.2	2.7	3.0	2.5
SIMO	1 × 2	4.2	3.7	3.9	3.4
SIMO	1 × 3	4.8	4.3	4.6	4.0
SIMO	1 × 4	5.2	—	5.0	—
MIMO	2 × 2	5.2	4.8	4.5	4.5
MIMO	3 × 3	7.3	6.9	5.7	6.6
MIMO	4 × 4	9.2	—	7.3	—

at random locations within our propagation environment. We then evaluate the tangent of the regression line that provides the best-fit estimate of the pathloss with distance on the log–log scale, which gives us the pathloss index  $n$  [15]. The scenario with  $K = 0$  represents freespace propagation with a single path, and thus  $n = 2$  as expected. With a more realistic value of  $K$ , such as  $K = 5$ , the pathloss index deviates from freespace behaviour. The observed values of the pathloss, along with the regression line, are shown in Fig. 6, from which the mean  $n$  is estimated as 1.73. This agrees with the values obtained from measurement: [28, 44] found  $n$  to be 1.7 in LOS UWB environments, while [26] reported  $n$  to be between 1.5 and 2. Also, the divergence of the simulated channel pathloss from its linear regression, representing the mean pathloss, is small, indicating the accuracy and consistency of the model in characterising the pathloss.

#### 4.5 Multiple-antenna capacity

Multiple-antenna, or MIMO, systems provide a linear increase in the spectral efficiency under favourable propagation conditions [45]. Thus, a MIMO system with UWB signalling can support spectacularly high information rates as demonstrated in [46]. A multiple-receiver, or single-input multiple-output (SIMO), system can also be used for capacity enhancement and is a special case of MIMO. We now apply our ray-tracing technique to predict MIMO performance in an indoor UWB channel. The capacity of an  $n_A \times n_B$  MIMO system,  $n_B > n_A$ , operating in a discrete frequency-selective channel without feedback is given by [47]

$$C = \frac{1}{n_F} \sum_{f=1}^{n_F} \log_2 \det \left\{ \mathbf{I}_{n_B} + \frac{\rho}{n_A} \mathbf{H}(f) \mathbf{H}^H(f) \right\} \quad (10)$$

where  $\rho$  is the average SNR at the receiving array,  $n_F$  is the number of frequency components in the signal,  $n_A$  and  $n_B$  denote the number of transmitting and receiving antennas, respectively,  $(\cdot)^H$  represents the Hermitian transpose, and  $\mathbf{H}(f) = [h_{ba}(f)]$  is the MIMO channel matrix such that  $h_{ba}(f)$  is the complex frequency transfer coefficient at frequency  $f$  relating the  $a$ th transmitting and  $b$ th receiving antenna. As is conventional in MIMO analysis,  $\mathbf{H}(f)$ , is normalised such that its squared Frobenius norm  $\|\mathbf{H}(f)\|_F^2 = n_A n_B$ . Uniform linear arrays with inter-element spacing of 6 cm are synthesised, and the MIMO channel is measured at random locations within the 6 m × 6 m room. The CIRs are generated by ray-tracing and converted to the frequency domain via the FFT so that they can be used for the calculation of the system capacity  $C$ . We then compute the first-order statistics of  $C$  over the ensemble of spatial

locations at  $\rho = 10$  dB and find that  $C$  increases approximately linearly with the array size when  $n_A = n_B$  in the indoor UWB channel even under LOS conditions and specular reflections. Also, the capacity obtained is found to have low variance due to the frequency diversity and low fading of UWB signals, as explained in [48]. The ergodic and outage capacities, defined in [47], are listed in Table 3, and show a reasonable match with multiple-antenna UWB measurements obtained in [9, 46] at the same SNR under LOS conditions in a room of the same size and with the same array inter-element spacing. Further analysis shows that the variance of MIMO capacity predicted by the ray-tracing model increases with the array size. As a result, the ray-tracing capacity probability density function becomes flatter at large  $n_A = n_B$ , so that the measured outage capacity exceeds that obtained with ray-tracing with large arrays. We can infer from this observation that specular reflection does not provide sufficient scattering required for linear growth in MIMO capacity with array size, a fact that is well known from information theoretic MIMO analysis. The ray-tracing approach that considers only wall reflections is therefore more accurate for reasonably small array sizes. Multiple-antenna channel measurement is a tedious process that requires expensive specialised hardware, and the proposed model can therefore be a useful tool for MIMO capacity prediction.

#### 4.6 Power convergence

Owing to the Friis transmission equation [15], a typical wireless channel has an exponentially decaying PDP.

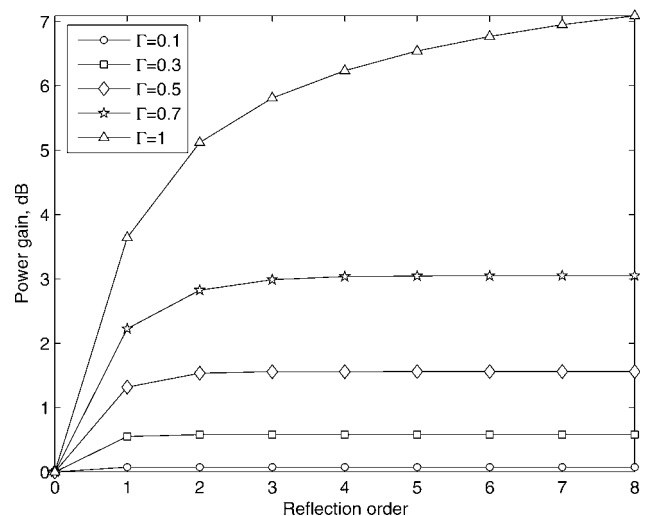


**Fig. 7** Convergence of received power with reflection order for various values of the wall reflection coefficient,  $\Gamma$

Thus, the fractional power gain with an increasing order of reflection in our simulation follows the law of diminishing returns, as higher order paths have greater pathlengths and lower energy. It was shown in [49] that  $K = 2$  provides sufficient information about large-scale channel variation, while [50] suggested that  $K = 3$  is sufficient for modelling indoor UWB propagation. Furthermore, [51] showed that the power level prediction improvement is lower than 3 dB beyond  $K = 3$ . From our results based on a large set of CIRs simulated with ray-tracing, it is found that the power gain converges to within 1 dB with increase in  $K$  beyond  $K = 1$  for  $\Gamma = 0.7$ , and  $K = 3$  for  $\Gamma = 1$ . This is illustrated with the help of Fig. 7. It can be concluded from this information that 3–4 reflections are sufficient to model the indoor UWB channel under typical conditions. As the value of  $K$  in the model is directly related to its runtime complexity, a low  $K$  providing reasonable simulation accuracy increases the raytracing efficiency.

## 5 Conclusion

An efficient deterministic modelling technique for indoor radio channels has been presented. The proposed time-domain technique uses the method of images to predict the ray paths and generate the CIR in a given propagation environment. The method has been applied to the prediction of the UWB indoor channel in the FCC frequency band, but is generic and can also be used at other microwave, millimetre-wave and optimal frequency ranges. The resulting CIRs are found to be in good agreement with channel measurement, with the multipath components arriving in rapid succession in the form of time-domain clusters. The small-scale fading statistics of the channel estimated from our simulation also agree with published measurement results. Further analysis of small-scale fading over a planar area, simulating the movement of a receiver and the consequent changes in the received signal characteristics, reveals the presence of spatial interference fringes formed due to the vector superposition of the impinging paths. The aperture synthesis used in the prediction of the spatial propagation characteristics in this paper is made possible by the low computational intensity of the technique. A grid-like angular symmetry is produced by multipath clusters in the ADP, due to the geometry of a rectangular room. Our analysis reveals that the indoor radio channel can be adequately modelled by up to three reflections, and the dominant mode of propagation is specular reflection from the walls. The linear scaling of MIMO capacity with array size predicted by the ray-tracing model confirms measurement-based analyses of indoor UWB channels. Thus, it has been shown that the ray-tracing scheme developed in this paper provides a convenient tool for the simulation of indoor electromagnetic signal propagation and system performance prediction.

## 6 Acknowledgment

This work was supported in part by the UK Engineering and Physical Sciences Research Council via Grant GR/T21769/01. The authors are grateful to Dr Dominic O'Brien and Dr Ben Allen for their valuable comments and suggestions.

## 7 References

- 1 Rizk, K., Wagen, J.F., and Gardiol, F.: 'Two-dimensional ray tracing modeling for propagation prediction in microcellular environments', *IEEE Trans. Veh. Technol.*, 1997, **46**, (2), pp. 508–518
- 2 Zhu, H., Takada, J.-I., Araki, K., and Kobayashi, T.: 'A ray-tracing-based characterization and verification of the

- spatio-temporal channel model for future wideband wireless systems', *IEICE Trans. Commun.*, 2001 **E48-B**
- 3 Kraus, J.D.: 'Electromagnetics' (McGraw-Hill, New York, USA, 1999, 5th edn.)
- 4 Döhler, M., Anna, M.D., and Aghvami, H.: 'A propagation model for the outdoor-indoor interface of the mobile radio environment'. Proc. Millenium Conf. Antennas Propagat. Davos, Switzerland, April 2000
- 5 Elnaggar, M., Safavi-Naeini, S., and Chaudhuri, S.K.: 'Effect of oversimplifying the simulated indoor propagation on the deterministic MIMO capacity'. Proc. Canadian Conf. Elect. Comp. Eng. Niagra Falls, Canada, May 2004
- 6 Tarrg, J.H., and Ju, K.M.: 'A novel 3-D scattering model of 1.8-GHz radio propagation in microcellular urban environment', *IEEE Trans. Electromag. Compat.*, 1999, **41**, (2), pp. 100–106
- 7 Son, H.-W., and Myung, N.-H.: 'A new approach to 3-D ray tracing for a microcellular propagation prediction model in urban environments', *Microw. Opt. Tech. Lett.*, 1999, **23**, (3), pp. 159–163
- 8 Bertoni, H., Honcharenko, W., Maciel, L.R., and Xia, H.: 'UHF propagation prediction for wireless personal communications', *Proc. IEEE*, 1994, **82**, (9), pp. 1333–1359
- 9 Allen, B., Dohler, M., Okon, E.E., Malik, W.Q., Brown, A.K., and Edwards, D.J. (Eds.): 'Ultra-wideband antennas and propagation for communications, radar and imaging' (Wiley, London, UK, 2006)
- 10 Sugahara, H., Watanabe, Y., Ono, T., Okanou, K., and Yamazaki, S.: 'Development and experimental evaluations of 'RS-2000' – a propagation simulator for UWB systems'. Proc. IEEE Int. Workshop Ultra Wideband Sys. joint with Conf. Ultra Wideband Sys. Tech, Kyoto, Japan, May 2004
- 11 Attiya, A.M., and Safaai-Jazi, A.: 'Simulation of ultra-wideband indoor propagation', *Microw. Opt. Tech. Lett.*, 2004, **42**, (2), pp. 103–108
- 12 Lawton, M.C., and McGeehan, J.P.: 'The application of a deterministic ray launching algorithm for the prediction of radio channel characteristics in small-cell environments', *IEEE Trans. Veh. Technol.*, 1994, **43**, (4), pp. 955–969
- 13 Wölfle, G., Hoppe, R., and Landstorfer, F.M.: 'A fast and enhanced ray optical propagation model for indoor and urban scenarios, based on an intelligent preprocessing of the database'. Proc. IEEE PIMRC, September 1999, Osaka, Japan
- 14 Athanasiadou, G.E., Nix, A.R., and McGeehan, J.P.: 'A microcellular ray-tracing propagation model and evaluation of its narrow-band and wide-band predictions', *IEEE J. Sel. Areas Commun.*, 2000, **18**, (3), pp. 322–335
- 15 Rappaport, T.S.: 'Wireless communications: principles and practice' (Prentice-Hall, 2001, 2nd edn.)
- 16 Hassan-Ali, M., and Pahlavan, K.: 'A new statistical model for site-specific indoor radio propagation prediction based on geometric optics and geometric probability', *IEEE Trans. Wirel. Commun.*, 2002, **1**, (1), pp. 112–124
- 17 Keenan, J.M., and Motley, A.J.: 'Radio coverage in buildings', *Br. Telecom. Technol. J.*, 1990, **8**, (1), pp. 19–24
- 18 Malik, W.Q., Edwards, D.J., and Stevens, C.J.: 'Frequency-dependent pathloss in indoor ultrawideband channels'. Proc. IEEE Int. Conf. Commun., Istanbul, Turkey, June 2006
- 19 Win, M.Z., and Scholtz, R.A.: 'Ultrawide bandwidth time-hopping spread-spectrum impulse radio for wireless multiple-access communications', *IEEE Trans. Commun.*, 2000, **48**, (4), pp. 679–691
- 20 Win, M.Z., and Scholtz, R.A.: 'Impulse radio: how it works', *IEEE Commun. Lett.*, 1998, **2**, (2), pp. 36–38
- 21 Malik, W.Q., Edwards, D.J., and Stevens, C.J.: 'Angular-spectral antenna effects in ultra-wideband communications links', *IEE Proc. Commun.*, 2006, **153**, (1), pp. 99–106
- 22 Muqaibel, A., Safaai-Jazi, A., Woerner, B., and Riad, S.: 'UWB channel impulse response characterization using deconvolution techniques'. Proc. IEEE Int. Midwest Symp. Circuits Systems, Tulsa, OK, USA, August 2002
- 23 Saleh, A.A.M., and Valenzuela, R.A.: 'A statistical model for indoor multipath propagation', *IEEE J. Sel. Areas Commun.*, 1987, **5**, (2), pp. 128–137
- 24 Win, M.Z., and Scholtz, R.A.: 'Characterization of ultra-wideband wireless indoor channels: a communication-theoretic view', *IEEE J. Sel. Areas Commun.*, 2002, **20**, (9), pp. 1613–1627
- 25 Foerster, J., and Li, Q.: 'UWB channel modeling contribution from Intel', *IEEE P802.15-02/279-SG3a*
- 26 Molisch, A.F.: 'Ultrawideband propagation channels – theory, measurement, and modeling', *IEEE Trans. Veh. Technol.*, 2005, **54**, (5), pp. 1528–1545
- 27 Rautiainen, T., Wölfle, G., and Hoppe, R.: 'Verifying path loss and delay spread predictions of a 3D ray tracing propagation model in urban environments'. Proc. IEEE Veh. Technol. Conf. Vancouver, Canada, September 2002

- 28 Ghassemzadeh, S.S., Jana, R., Rice, C.W., Turin, W., and Tarokh, V.: 'Measurement and modeling of an ultra-wide bandwidth indoor channel', *IEEE Trans. Commun.*, 2004, **52**, (10), pp. 1786–1796
- 29 Keignart, J., and Daniele, N.: 'Subnanosecond UWB channel sounding in frequency and temporal domain'. Proc. IEEE Conf. Ultra-Wideband Sys. Tech, Baltimore, MD, USA, May 2002
- 30 Malik, W.Q., Edwards, D.J., and Stevens, C.J.: 'Frequency dependence of fading statistics for ultrawideband systems', *IEEE Trans. Wirel. Commun.*, 2007, **6**, (3), pp. 800–804
- 31 Siwiak, K., Bertoni, H.L., and Yano, S.M.: 'Relation between multipath and wave propagation attenuation', *Electron. Lett.*, 2003, **39**, (1), pp. 142–143
- 32 Molisch, A.F., Foerster, J.R., and Pendergrass, M.: 'Channel models for ultrawideband personal area networks', *IEEE Wireless Commun.*, 2003, **10**, (6), pp. 14–21
- 33 Varela, M.S., Sanchez, M.G., Lukama, L., and Edwards, D.J.: 'Spatial diversity analysis for digital TV systems', *IEEE Trans. Broadcast.*, 2001, **47**, (3), pp. 198–206
- 34 Malik, W.Q., Edwards, D.J., and Stevens, C.J.: 'Optimal system design considerations for the ultra-wideband multipath channel'. Proc. IEEE Veh. Technol. Conf, Dallas, TX, USA, September 2005
- 35 Hansen, J.: 'A novel stochastic millimeter-wave indoor radio channel model', *IEEE J. Sel. Areas Commun.*, 2002, **20**, (6), pp. 1240–1246
- 36 Sklar, B.: 'Rayleigh fading channels in mobile digital communication systems, part I: characterization', *IEEE Commun. Mag.*, 1997, **35**, (7), pp. 90–100
- 37 Hecht, E., and Zajac, A.: 'Optics' (Addison-Wesley, London, UK, 2001, 4th edn.)
- 38 Haykin, S.: 'Array signal processing' (Prentice-Hall, Englewood Cliffs, NJ, USA, 1985)
- 39 Durgin, G.D., and Rappaport, T.S.: 'Effects of multipath angular spread on the spatial cross-correlation of received voltage envelopes'. Proc. IEEE Veh. Technol. Conf, Houston, TX, USA, May 1999
- 40 Cramer, R.J.-M., Scholtz, R.A., and Win, M.Z.: 'Evaluation of an ultra-wide-band propagation channel', *IEEE Trans. Antennas Propag.*, 2002, **50**, (5), pp. 561–570
- 41 Malik, W.Q., Stevens, C.J., and Edwards, D.J.: 'Synthetic aperture analysis of multipath propagation in the ultra-wideband communications channel'. Proc. IEEE Workshop Signal Processing Advance Wireless Commun, New York, USA, June 2005
- 42 Prettie, C., Cheung, D., Rusch, L., and Ho, M.: 'Spatial correlation of UWB signals in a home environment'. Proc. IEEE Conf. Ultra-Wideband Sys. Tech, Baltimore, MD, USA, May 2002
- 43 Denis, M., Vasudevan, V., Chandra, K., and Thompson, C.: 'Characterizing spatial correlation in indoor channels'. Proc. IEEE Wireless Commun. Net. Conf, Atlanta, GA, USA, March 2004
- 44 Cassioli, D., Durantini, A., and Ciccognani, W.: 'The role of path loss on the selection of the operating bands of UWB systems'. Proc. IEEE Int. Symp. Personal Indoor Mobile Radio Communication, Barcelona, Spain, September 2004
- 45 Telatar, I.E., and Tse, D.N.C.: 'Capacity and mutual information of wideband multipath fading channels', *IEEE Trans. Inform. Theory*, 2000, **46**, (4), pp. 1384–1400
- 46 Malik, W.Q., and Edwards, D.J.: 'Measured MIMO capacity and diversity gain with spatial and polar arrays in ultrawideband channels', *IEEE Trans. Commun.*, in press
- 47 Paulraj, A.J., Nabar, R., and Gore, D.: 'Introduction to space-time wireless communications' (Cambridge University Press, Cambridge, UK, 2003)
- 48 Molisch, A.F., Steinbauer, M., Toeltsch, M., Bonek, E., and Thomä, R.S.: 'Capacity of MIMO systems based on measured wireless channels', *IEEE J. Sel. Areas Commun.*, 2002, **20**, (3), pp. 561–569
- 49 Dardari, D., Minelli, L., Tralli, V., and Andrisano, O.: 'Fast ray-tracing characterization of indoor propagation channels at 60 GHz'. Proc. IEEE Veh. Technol. Conf, Phoenix, AZ, USA, May 1997
- 50 Kunisch, J., and Pamp, J.: 'Measurement results and modeling aspects for the UWB radio channel'. Proc. IEEE Conf. Ultra-Wideband Sys. Tech, Baltimore, MD, USA, May 2002
- 51 Valenzuela, R.A., Fortune, S., and Ling, J.: 'Indoor propagation prediction accuracy and speed versus number of reflections in image-based 3-d ray-tracing'. Proc. IEEE Veh. Technol. Conf, Ottawa, Canada, May 1998